Heliyon 10 (2024) e30109

Contents lists available at ScienceDirect

Heliyon

journal homepage: www.cell.com/heliyon

Research article

Comprehensive first principles to investigate optoelectronic and transport phenomenon of lead-free double perovskites Ba_2AsBO_6 (B═Nb, Ta) compounds

Mumtaz Manzoor [a], Debidatta Behera [b], Ramesh Sharma [c], A.J.A. Moayad [d,*], Abdullah A. Al-Kahtani [e], Yedluri Anil Kumar [f]

[a] Institute of physics, Slovak Academy of Science, Dubravska Cesta 9, 84507, Bratislava, Slovakia
[b] Department of Physics Birla Institute of Technology, Mesra, Ranchi, 835215, Jharkhand, India
[c] Department of Applied Science, Feroze Gandhi Institute of Engineering and Technology, Raebareli, 229001, Uttar Pradesh, India
[d] Department of Materials Science, Malawi University of Science and Technology P.O Box 5196, Limbe, Malawi
[e] Department of Chemistry, College of Science, King Saud University, P. O. Box 2455, Riyadh, 11451, Saudi Arabia
[f] Saveetha School of Engineering, Saveetha Institute of Medical and Technical Sciences, Saveetha University, Chennai, 602105, Tamilnadu, India

ARTICLE INFO

Keywords:
Double perovskite (DP)
Structural properties
Elastic properties
Electronic properties
Transport properties

ABSTRACT

In the current work we studied the structural, elastics, electrical, optical, thermoelectric, as well as spectroscopic limited maximum efficiency (SLME) of oxide based Ba_2AsBO_6 (B═Nb, Ta) materials. All the calculations were performed using first-principles calculation by employing the WIEN2k code. We checked the stability in diverse forms such as optimization, phonon dispersion, mechanical, formation energy, cohesive energy, and thermal stability is computed. The semiconducting nature of these Ba_2AsBO_6 (B═Nb, Ta) systems is revealed by calculating the direct band gap values are 1.97 eV and 1.49 eV respectively. Additionally, we determined the optical properties which analyze the utmost absorption and transition of carriers versus photon energy (eV). Moreover, Ba_2AsNbO_6 has an estimated SLME of 32 %, making it an encouraging alternative for single-junction solar cells. Lastly, we studied the transport properties against temperature, the chemical potential for p-type and n-type charge carriers at various temperatures. At 300 K, the zT values are found to be 0.757 and 0.751 for Ba_2AsBO_6 (B═Nb, Ta) compounds respectively. Both materials were examined as having strong absorption patterns and an excellent figure of merit (ZT), indicating that materials are appropriate for daily life applications.

1. Introduction

The energy disaster, which has arisen because of the degradation of worldwide energy supplies, has prompted researchers to evaluate other techniques, such as conversion of waste-heat energy into electrical energy. The application as well as collection of the renewable energy resources for instance solar as well as thermal energy, are potentially appeared in the solid-state devices [1–3]. The researcher community faces lots of difficult problems in discovering high efficiency, cost-effective, and environmentally non-threatening solid materials. The perovskites solids have been broadly studied in this context because of their use on high rank of industrial devices, involving photo-catalyst phototransistors, ferroelectric and piezoelectric metals, LEDs, high-temperature

* Corresponding author.
E-mail address: mailme_moya123@rediffmail.com (A.J.A. Moayad).

https://doi.org/10.1016/j.heliyon.2024.e30109
Received 23 November 2023; Received in revised form 18 April 2024; Accepted 19 April 2024
Available online 20 April 2024

superconductors, magneto resistances, and solar systems [3–11]. Oxygen based double perovskites had been reported experimentally having the high the bandgap nature. Consequently, these chemicals weren't suitable for solar applications. Several attempts have been made in the past ten years to increase the effectiveness of photo-electro-chemical devices to create organic-inorganic hybrid composites, or solids that combine an organic molecule with a lead halogen perovskite [12–15]. Nevertheless, excess moisture, temperature, and other variables cause Pb-based halide perovskite to lose efficiency, which is its main drawback [16,17]. The other demerit is the toxicity of lead [16–22]. Furthermore, halide vacancy migration makes these solids not extremely stable [22–24]. Consequently, the focus of the scientific community has shifted to the identification of solids that are safe for the environment, stable at room temperature, and capable of being produced efficiently over an extended period. To solve this problem, several attempts to replace lead atoms with Sn/Ge atoms have been made; however, these atoms oxidize in the atmosphere, limiting the device's life [25,26]. To overcome all problems, we studied oxygen based double perovskites materials by replacing the Ta with Nb.

To overcome the practical difficulties, which are related with these substances, the scientists investigated DP materials with a general formula of $A_2BB'C_6$, where A site atoms may be alkali metals, B-atoms may be lanthanide series atoms, and C-atoms are commonly oxygen or halogen atoms [27–29]. The use of DP materials in ferroelectric, ferromagnetic, and other uses has been demonstrated [30–33]. In this regard, McClure et al. [33,34] produced the Cs_2AgBiX_6 (X = Cl, Br, and I) compounds with a DP structure as well as studied their electrical and optical characteristics. In comparison to other compounds, the researchers observed that double perovskites are extremely efficient and stable, making them ideal for photo-electrochemical cells. Volonakis et al. [35] investigated photoelectric characteristics of these materials $Cs_2B'B''X_6$ (B′ = Bi, Sb; B″ = Cu, Ag, Au; as well as X = Cl, Br, I) and discovered they display variable electronic band gaps that lie in visible region and has a low carrier effective mass. $Cs_2InAgCl_6$, $Cs_2InAgBr_6$, Cs_2InAg $(Cl_{1-x}Br_x)_6$, as well as Cs_2AgIO_6 are all double perovskite compounds that have newly been produced. According to the theoretical study of double perovskite materials are promising renewable energy sources because of these materials have a straight semiconducting nature [36–38]. Zhou et al. studied Mn-doped $Cs_2NaBi_{1-x}In_xCl_6$ and investigated its electrical and optical characteristics. The shift from indirect to direct bandgap behavior was discovered to be caused by the surge in Bi doping carriers at the In. As indicated by the above investigations, various research groups have worked hard to comprehend the crucial challenge of the DP $A_2BB'X_6$ optoelectronic capabilities. The investigators were attempting to uncover variations in optoelectronic characteristics by replacing A, B, and B′ with other elements. For appealing application of optoelectronics, Syed. M. Alay-e-Abbas et al. published the 2D A_3SnO (A = Ca, Sr, and Ba) anti-perovskites monolayer [39]. Abhishek Sharan et al., reported about the sustainable energy by using the ternary compounds FeX_2Y_4 (X = Ga, In and Y═S, Se, Te) [40]. To use optoelectronic and thermal devices, Mumtaz et al., reported the many theoretically perovskites and double perovskites materials [41–45]. To check the stability and nature of transport characteristics of TiB_2 and ZrB_2 monolayers by employing the strain studied by shubham Tygi et al., in 2023 [46,47]. Hussian et al. studied the La_2CoMnO_6 perovskite compounds and revealed their application in optoelectronics devices [48]. Tb_2MnCoO_6 compound is studied by Khailil et al. and suggested the dynamical stability of the compound as well as its usage in optoelectronics devices [49]. For the $LBaMn_2O_6 - \gamma$ (L = Pr, Nd, Sm, Eu, Gd, and Tb) series, Trukhanov et al. [50]. concentrated on the structural, magnetic, as well as thermal characteristics. The motivation of these materials is in its unique crystal structure, tunable properties, and potential uses into diverse fields involving optoelectronics, catalysis, as well as energy storage. The aim of studying these materials theoretically is to calculate the electronic and transport properties pf Ba_2AsBO_6 (B═Nb, Ta) for use of optoelectronic and thermal devices.

We executed the full potentials linearized augmented plane waves (FP-LAPW) employing the different approximations. Relied on the first-principles study, we considered the structural, elastic, electronics, optical, as well as thermoelectric characteristics versus temperature, chemical potential, as well as carrier concentrations of lead-free DP materials Ba_2AsBO_6 (B═Nb, Ta) respectively.

2. Computational details

The VESTA software [51] executed to envision the crystal structure of Ba_2AsBO_6 (B═Nb, Ta) the double perovskites. The WIEN2k [52] code used to compute structural, mechanical properties of Ba_2AsBO_6 (B═Nb, Ta) materials utilizing the Perdew-Burke-Ernzerhof (PBE) approaches inside the density functional theory (DFT) [53]. The equation of PBE + GGA is

$$E_{xc}[\rho] = \int \rho(\boldsymbol{r})\epsilon_{xc}(\rho(\boldsymbol{r}), \nabla\rho(\boldsymbol{r}))dr \tag{1}$$

$E_{xc}[\rho]$ = exchange-correlation energy functional.
$\rho(\boldsymbol{r})$ = electron density
$\nabla\rho(\boldsymbol{r})$ = gradient of the electron density
$\epsilon_{xc}(\rho, \nabla\rho(\boldsymbol{r}))$ = exchange-correlation energy per particle.

The equation of PBE + GGA + mBJ is $V_{XC}^{mBJ} = V_{XC}^{LDA} + \Delta V_{XC}^{mBJ}$ In addition, modified Becke-Johnson (mBJ) exchange approximation was considered to get the more exact electrical and optical characteristics of the materials [54,55]. The FP-LAPW approach splits space into two parts: the interstitial portion as well as un-overlapping muffin tin (MT) spheres. The MT radii for Ba, Sb, Nb, Ta, and O atoms computed to be 2.45, 1.90, 1.87, 2.02, as well as 1.62 atomic units (a.u.). In the unit cell, the smallest muffin tin radius is R_{MT}, we tried to set the plane wave cut-off value $K_{max}*R_{MT} = 8$, and $G_{max} = 12$ was set as the maximum Fourier expansion of charge density. The 10 × 10 × 10 grid was used to integrate the reciprocal space of the irreducible Brillouin zone and also a total of 1000 k-points were used. The total convergence with E_c of material 10^{-5} Ry used whole the self-consistent computations. The IRelast package has been executed to compute elastic properties of the investigated compounds. We applied BoltzTrap algorithm [56] to reveal the transport properties. Rigid band approximation (RBA) and constant relaxation time approximation are used (CRTA). We assumed that the band remains

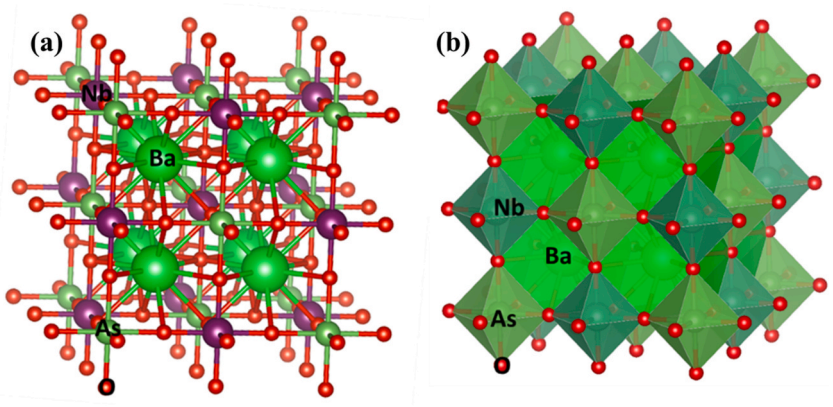

Fig. 1. Generated the cubic crystal structure of Ba_2AsBO_6 (B═Nb, Ta) compounds in (a) stick-ball and (b) polyhedral respectively.

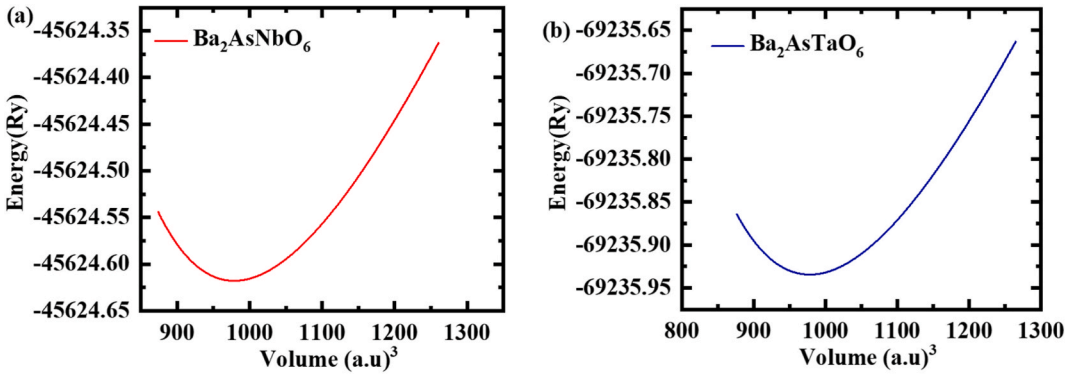

Fig. 2. Calculated the (a, b)ground-stated energyof Ba_2AsBO_6 (B═Nb, Ta) compounds by optimizationas a function of Volume (a.u)^{3}correspondingly.

Table 1
Calculated lattice parameter *a* (A°), bulk modulus *B*, its derivative B_P, the minimum total energy E_{tot}, energy of cohesion E_{coh}, enthalpy of formation E_f and bondlength **(Å)**.

Compounds	a (Å)	V(a.u^3)	B (GPa)	B.P	E_{tot}(Ry)	E_c (eV/atom)	E_f(eV/atom)	Bond length (Å)	Bader Charges
Ba_2AsNbO_6	8.3417	979.27	150.48	4.77	−45624.617651	5.86	−2.743	Ba–As = 3.5906 Ba–Nb = 3.5906 Ba–O = 2.9327	Ba = 1.5759 As = 1.7234 Nb = 2.5386 O = −1.234
Ba_2AsTaO_6	8.3397	978.56	154.37	4.65	−69235.934265	5.53	−2.853	Ba–As = 3.5955 Ba–Ta = 3.5955 Ba–O = 2.9367	Ta = 2.6324 O = −1.2513
Ref [60].	8.192	980.14	469.31	4.72	−49604.71				

identical to chemical potential changes. Additionally, the relaxation duration was energy individual [54,57].

3. Result and discussion

3.1. Structure properties

To begin our extensive examination [58]with the many characteristics of Ba_2AsBO_6 (B═Nb, Ta) materials. They have optimal lattice values of 8.3417 as well as 8.3397 correspondingly. Ba_2AsBO_6 (B═Nb, Ta) compounds have a cubic structure with the space group # 225, Fm3m. Having the Ba, Sb, Nb/Ta, and O atoms occupying positions 8c (0.25, 0.25), 4a (0, 0, 0), 4b (0.5, 0, 0), and 24e (x, 0, 0). Fig. 1 (a, b) depicts the unit cell of Ba_2AsBO_6 (B═Nb, Ta) in stickball and polyhedral style. We used the PBE functional to optimal the structural parameters for both solids with Murnaghan equation of state against volume (a.u) as shown in Fig. 2 (a, b). All structural parameters and bond length of oxygen based double perovskites Ba_2AsBO_6 (B═Nb, Ta) materials are specified in Table 1. Additionally,

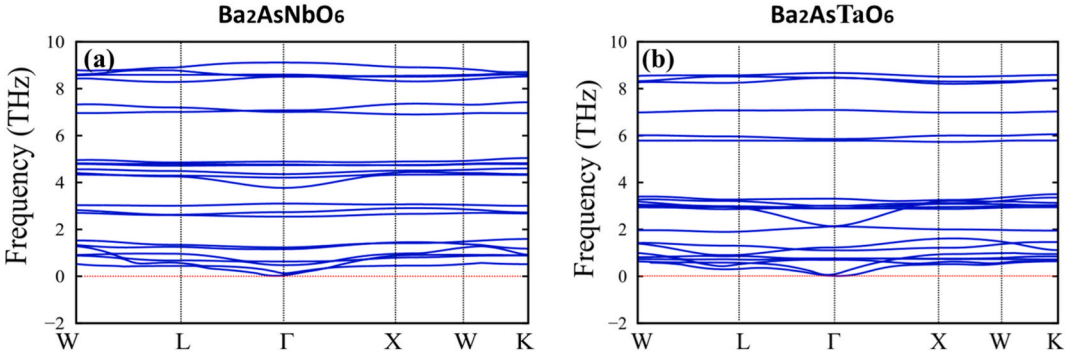

Fig. 3. To check the dynamical stability of double perovskites, we calculated the phonon dispersion of (a) for $Ba_2As\ NbO_6$ and (b) for Ba_2As-TaO_6 compounds.

Table 2
Calculated values of elastic constants C_{11}, C_{12}, C_{44} in (GPa), bulk modulus B (GPa), shear modulus G (GPa), Young's modulus Y (GPa), Poisson's ratio ν, Zener anisotropy factor (A), B/G ratio, Cauchy pressure (C_{12}–C_{44}) and melting temperature Tm (K) for Ba_2AsBO_6 (B═Nb, Ta) compounds.

Parameters	Ba_2AsNbO_6	Ba_2AsTaO_6	Other study [70]
$\mathbf{C_{11}}$	257.10	258.31	251.82
$\mathbf{C_{12}}$	100.30	104.70	78.77
$\mathbf{C_{44}}$	82.53	83.89	61.90
B	152.57	155.91	136.46
G	80.88	81.06	70.80
Y	206.20	207.25	188.89
ν	0.2747	0.2784	0.28
B/G	1.75	1.76	1.93
A	1.052	1.092	0.72
$\mathbf{\Theta_D}$	492.9	498.8	
$\mathbf{V_{tran}}$	3635	3378	
$\mathbf{V_{long}}$	6523	6098	
Vavg.	4048	3763	
$\mathbf{T_m}$	3128	3146	

observed computed lattice constants of Ba_2AsNaO_6 are higher as compared to the Ba_2AsTaO_6 which might be related to the atom conditional variance [59]. The computed average bond length can be spent to estimate tolerance factor, as well as thus crystal structure of the compound has been projected. Temperature and pressure influence the tolerance factor. The tolerance factor value of 0.95–1.04 with the analytically derived values, indicating that the compound has a cubic structure. The tolerance factor of studied compounds are around one for the cubic structure of the investigated Ba_2AsBO_6 (B═Nb, Ta) compounds.

For materials stability, we calculated the formation and cohesive energy which are given in Table 1. Their mathematical expression is written in equations (1) and (2)

$$E_f = E_{Total}^{XInO3} - E_X^{bulk} - E_{In}^{bulk} - 3E_O^{bulk} \tag{2}$$

$$H_{coh} = E_X^{bulk} + E_{In}^{bulk} + 3E_O^{bulk} - E_{Total}^{XInO3} \tag{3}$$

3.2. Phonon dispersion

To analyze dynamical stability of DP Ba_2AsBO_6 (B═Nb, Ta) compounds in bulk form, we computed the phonon calculation having the frequency along y-axis and vastly symmetric K wave vector [W, L, Γ, X, W, K] in the Brillion zone along x-axis as demonstrated in Fig. 3 (a, b). There are two types of the mode's longitudinal modes and optical modes, longitudinal modes lie in low frequency, but optical modes lie in high frequency as compared to longitudinal modes. Fig. 3 (a) shows the phonon dispersion for for $Ba_2As\ NbO_6$ and Fig. 3 (b) for $Ba_2As\ TaO_6$ compound. From these figures, it is analyzed that whole vibrational branches lie in the real frequency rather than imaginary frequency. Having the positive frequency advocated the materials are dynamically stable nature.

3.3. Elastic properties

Elastics qualities are important when constructing solids for practical production on behalf of different applications. We computed the Second-order elastic constants (C_{ij}), such as Young's modulus (Y), Poisson's ratio(v), bulk modulus (B), shear modulus (G),

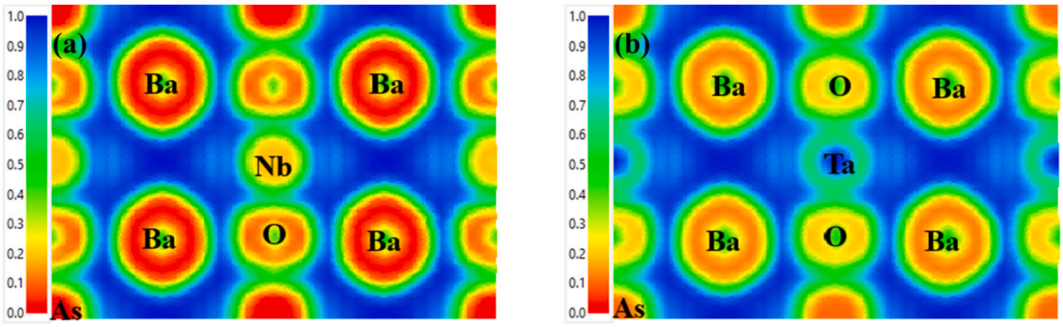

Fig. 4. Considered the electron localization of double perovskites (a, b) Ba_2AsBO_2 (B═Nb, Ta) respectively.

brittleness, ductility, anisotropy, elastic wave propagation, Debye temperature, average velocity, longitudinal and transvers waves [54,61]. Three different elastic constantsC_{11}, C_{12}, and C_{44} are used to quantify the strength of the dimensional structure in the cubic system. Where C_{11} symbolizes the resistance of solids to shear bend, C_{12} represents shear stress, and C_{44} indicates opposition to shear deformation. Parameters obtained from the matrix of equations as well as also ought to be fulfill born elastic solidity forms [62], $(C_{11}–C_{12})/2 > 0$, $(C_{11}+2C_{12}) > 0$, $C_{11} > 0$ and $C_{44} > 0$. Our computed values elastic constants for Ba_2AsBO_6 (B═Nb, Ta) compounds are listed in GPa in table-2. These results meet the born elastic stability criterion, indicating that these compounds are mechanically stable. Furthermore, for both compounds tested, the values of Cauchy pressure, which would be the disparity among C_{11}, $C_{12,}$ and C_{44} [63], are positive [64,65]. This thing demonstrated that there is a metal nature in our structures. The resistance of a material to volume alter is measured by its isotropic bulk modulus (B). We employed the C_{11} and C_{12} elastic constants in Voigt-Russell-Hills estimates [66–69] to calculate the Bulk modulus. It can be expressed mathematically by the relationship,

$$B = \frac{C_{11} + 2C_{12}}{3} \tag{4}$$

Table-2 presents all computed properties for Ba_2AsBO_6 (B═Nb, Ta), including B, *B*'. When contrasted to Ba_2AsTaO_6, B of Ba_2AsNbO_6 shows less volume variation. Shear modulus can be used to describe hardness and resistance to changeable strain (G) [71], which may be used to compute the shear modulus.

$$G = \frac{1}{2} + (G_R - G_V) \tag{5}$$

Where, the upper and lower Gs are demonstrated by G_V and G_R correspondingly. Elastic constants may be used to calculate G_V and G_R [71]. Following expression,

$$G_V = \frac{C_{11} - C_{12} + 3C_{44}}{5} \tag{6}$$

$$G_R = \frac{5(C_{11} - C_{12})C_{44}}{3(C_{11} - C_{12}) + 4C_{44}} \tag{7}$$

The shear modulus of Ba_2AsTaO_6 (81.06 GPa) is greater than Ba_2AsNbO_6 (80.88 GPa), indicating that Ba_2AsTaO_6 is utmost rigid as compared to the Ba_2AsNbO_6 compound. The E for Ba_2AsBO_6 (B═Nb, Ta) is determined using mathematically [71], which combines bulk and shear modulus.

$$E = \frac{9PG}{3B - G} \tag{8}$$

Ba_2AsNbO_6 has a greater E value as compared to Ba_2AsTaO_6 resulting in better resistance to uniaxial stress in contrast to Ba_2AsNbO_6. Furthermore, any material brittle and ductile properties must be addressed for effective device construction. ν [72] as well as (B/G) help elaborate on this.(B/G) as well as they may be calculated using the following formula:

$$\nu = \frac{3B - E}{6B} \tag{9}$$

The B/G ratio determines physical qualities such as brittleness, ductility, direction, stiffness, and so on. If the B/G values are more than 1.75, correspondingly [73,74], the solid said to be ductile and acceptable for gadget construction. The material is brittle if the value is less than 0.26, while it is plastic if the value is larger than 0.26. Table 2 show the B/G values for Ba_2AsBO_6 (B═Nb, Ta) compounds. Those values indicate that these materials tested are ductile and therefore applicable for device manufacturing. Moreover, the “A" obtained from Eq. (9) is smaller than one, indicating that both solids are anisotropic [75,76].

Table 3
– Calculated energy bandgap (in eV) by different potentials PBE, mBJ, and mBJ + soc.

Properties	PBE	mBJ	mBJ + SOC
Ba_2AsNbO_6	1.355	1.492	1.466
Ref. [70]	1.48	1.80	1.80
Ba_2AsTaO_6	1.990	2.498	2.332
Ref [77].	1.93	2.69	2.44

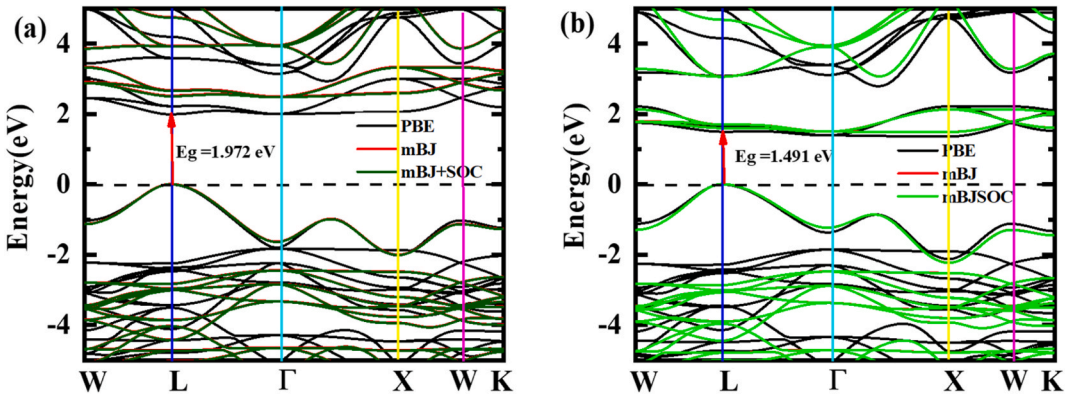

Fig. 5. Computed the electronic properties with (a and b) band structure is of Ba_2AsBO_6 (B═Nb, Ta) compounds respectively.

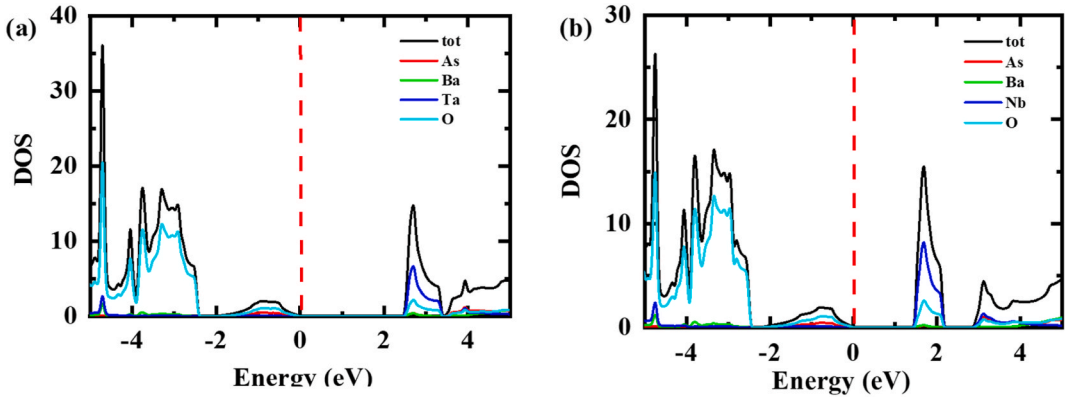

Fig. 6. Calculated the electronic properties with (a and b) TDOS and PDOS is of Ba_2AsBO_6 (B═Nb, Ta) compounds correspondingly.

$$A = \frac{2C_{44}}{C_{11} - C_{12}} \tag{10}$$

3.4. Electron localization function and Bader charges

To study the bonding, charge density as well as its spatial distribution could be used. There is no charge in ionic bonding; however, metallic, and covalent bonding have charge sharing among atoms. In a covalent bond, charge sharing was turned, whereas charge distribution is uniform through metallic bonding. Fig. 4 (a,b) illustrates the spatial charge concentration for the O-based DP along body diagonal plane. Ba as well as As atoms have completely spherical charge distributions, with no charge contours overlapping those of the O atom. This demonstrated that the Ba and As atoms have an ionic bond with O atom. On the other hand, Nb/Ta has exhibited covalent bonding with O atom because charge distribution differs from perfect spherical to distorted (dumb-bell type). This is also confirmed to Bader charge analysis and their values are given in Table-2. It is confirmed that O accepts electrons from Nb/Ta network due to covalent characteristics.

3.5. Electronic properties

To examine solid's nature, we considered fundamental characteristics of Ba_2AsBO_6 (B═Nb, Ta) materials in form of electronic band

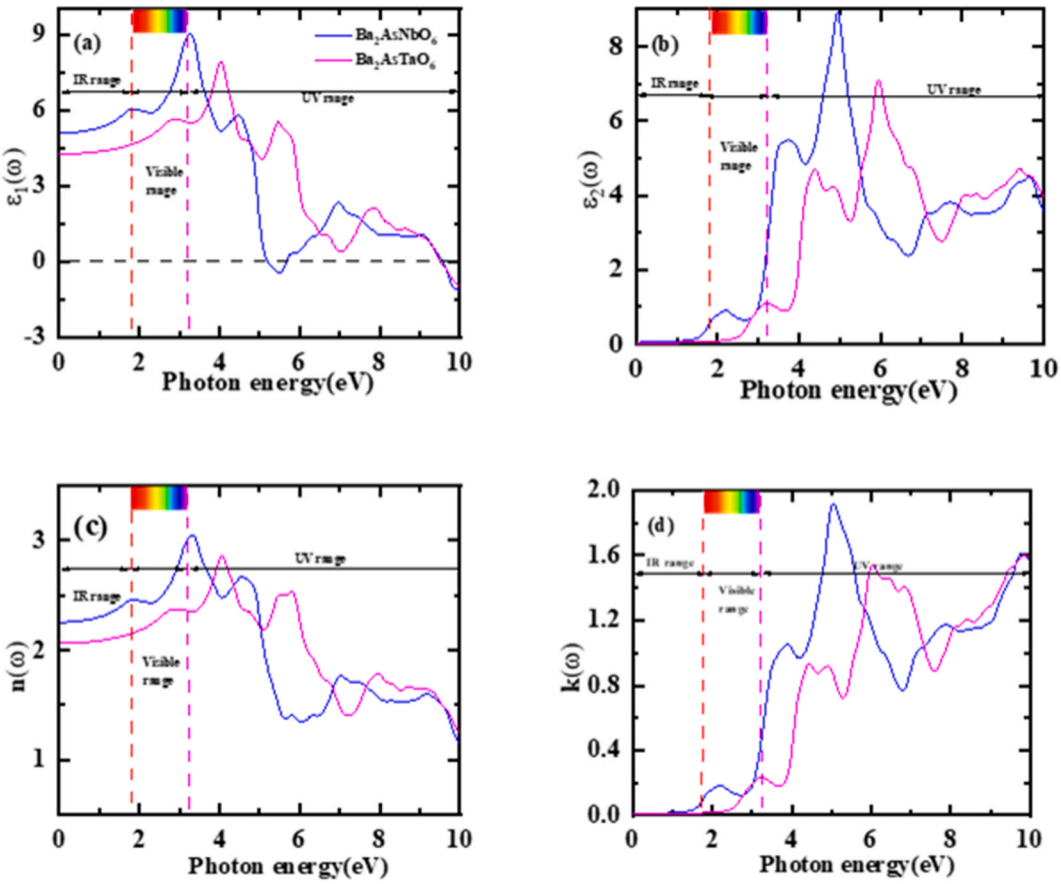

Fig. 7. Calculated the optical properties of with (a) real dielectric function (b) imaginary dielectric function (c) refractive index and (d) extinctioncoefficient as compared to photon energy (eV) Ba_2AsBO_6 (B═Nb, Ta)compounds correspondingly.

structures (BS), total, and partial densities of states (DOS). We used/executed diverse approximations like PB-WC, PBE, PBE + mBJ, and mBJ + soc to calculate the accurate band structure as well as DOS for both substances. Table-3 summarized the all-energy gaps determined from all approaches and previous data. The calculated energy band diagrams for Ba_2AsBO_6 (B═Nb, Ta) materials correspondingly. The computed energy bandgap for Ba_2AsNbO_6 with three approximations are1.35 eV, 1.49 eV and 1.466 eV, and for Ba_2AsTaO_6 are 1.99 eV, 2.498 eV, and 2.33 eV correspondingly, which rises to 1.49 eV and 2.49 eV when PBE + mBJ is used. Additionally, both solids have a direct bandgap character because of same highly symmetry K-points (can be seen) in Fig. 5 (a, b).

Besides this, we presented the amalgamated TDOS and PDOS of Ba_2AsBO_6 (B═Nb, Ta) materials in Fig. 6 (a, b). We show the DOS of Ba_2AsBO_6 (B═Nb, Ta) materials employing the PBE + mBJ interaction for a detailed look at energy bands. Moreover, the TDOS plotted with the energy range of -5eV to 5 eV are predominantly created by the O-electrons of Nb atoms but with tiny additions from the As atoms, correspondingly, as shown in Fig. 6 (a, b). In the valence band, just below the Fermi level [E_F], the 5s and 2s electrons of the As and O atoms can be observed. The 5s and 5d electrons of Nb/Ta atoms, 5p electrons of As atoms, 6s electrons of Ba atoms, and 2s electrons of O-atoms form the energy levels in the bottom conduction band. The majority of states in the energy range −5 eV–5 eV are made up of 4d subshells of Nb/Ta, 6s subshells of Ba, and 5p subshells of as atoms, with small additions from 5p-subshells of Nb/Ta and 5s-subshells of As atoms.

3.6. *Optical properties*

The dielectric function of any material may be used to analyze its dielectric reaction. It's important to note that every matter's dielectric function may be represented as [78].

$$(\omega) = \varepsilon_1(\omega) + i\varepsilon_2(\omega) \tag{11}$$

Where, $\boldsymbol{\varepsilon}_1(\boldsymbol{\omega})$ and $\boldsymbol{i\varepsilon}_2(\boldsymbol{\omega})$ are the real and imaginary components of the dielectric function respectively [79]. To investigate the optical properties, we calculated the optical properties with $\boldsymbol{\varepsilon}_1(\boldsymbol{\omega})$, $\boldsymbol{\varepsilon}_2(\boldsymbol{\omega})$, n ($\boldsymbol{\omega}$), and k ($\boldsymbol{\omega}$) respectively as shown in Fig. 7(a–d). Fig. 7(a and b) illustrates the real and imaginary part of a dielectric matrix as a function of photon energy (0 eV–10 eV) for both materials. The static point of the actual component with the dielectric permittivity for Ba_2AsBO_6 (B═Nb, Ta) compounds started roundabout from 5.08 to

Table 4
Calculated Optical and transport properties at room temperature.

	Material property	Ba_2AsNbO_6	Other works [68]	Ba_2AsTaO_6	Other works [85]
Optical properties	$\varepsilon_1(0)$	5.08	4.20	4.24	4.50
	R(0)	0.14	0.12	0.12	0.13
	$n(0)$	2.25	2.05	2.06	2.12
Transport properties (300K)	$\sigma/\tau(\Omega ms)^{-1}(10^{18})$	1.17	2.05	1.18	0.6
	S(μVK	242.5	145	239	240
	$PF(10^{11})$ (W/K^{2}ms)	0.89	3.0	0.89	3.1
	ZT_e	0.757	0.72	0.751	0.71 [86,87]

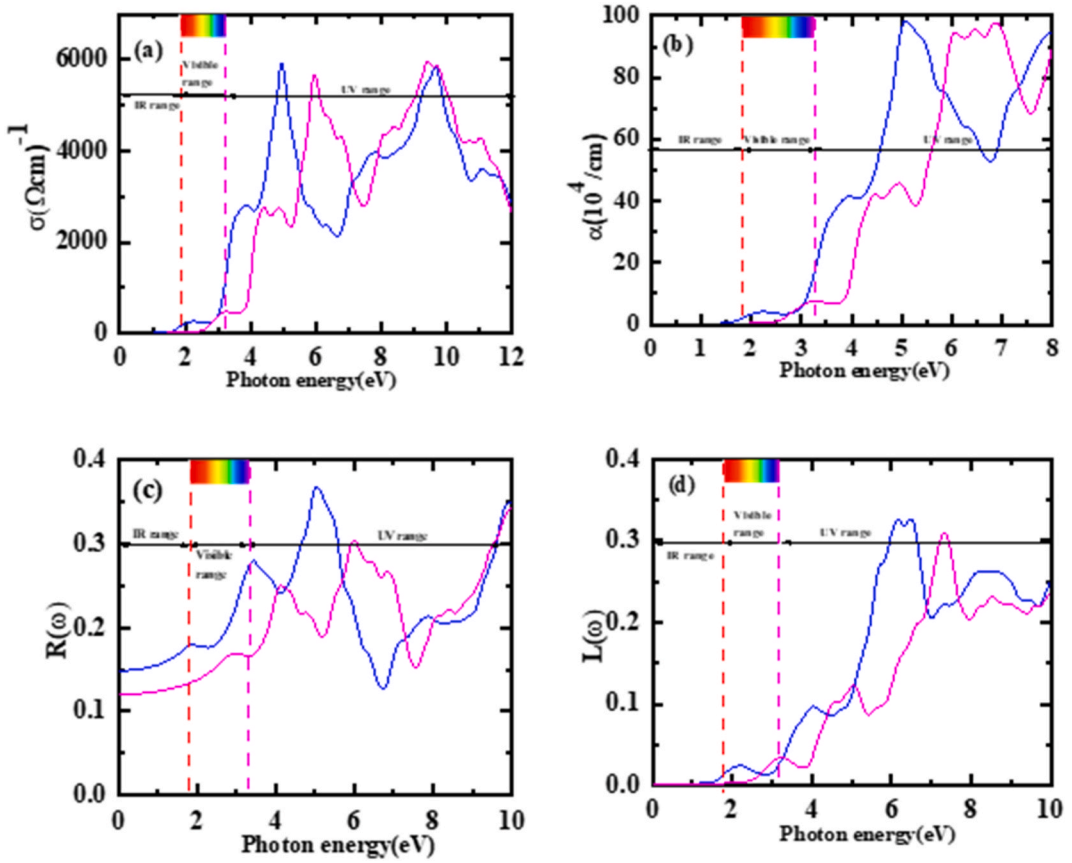

Fig. 8. Shows the (a) electrical conductivity (b) absorption coefficient (c) Reflectivity, and (d) energy loss for both Ba_2AsBO_6 (B═Nb, Ta) compounds correspondingly.

4.28 respectively and given in Table 4. According to the Penn model [65], the static constant $\varepsilon_1(0)$ for Ba_2AsNbO_6 and Ba_2AsTaO_6 is 5.08 and 4.28 respectively as shown in Fig. 7 (a). Further, by surging the energy in form of photon energy (eV) the transition of electrons from the valence to conduction increased till the visible region for Ba_2AsNbO_6 however for Ba_2AsTaO_6 increases in the ultraviolet region. Full potential LAPW band structure simulations were used to calculate the optical response of high-temperature superconductors [78,80,81]. Fig. 7 (b) presents the imaginary dielectric function to analyze the absorption factor by increasing the photon energy (eV). The static point values of $\varepsilon_2(0)$ are examined at zero for both compounds. Meanwhile, we observed the absorption in the visible region for both compounds as shown in Fig. 7 (b). These variations are caused by numerous inter-band transitions between the valence and conduction bands. Fundamental absorption edge values are those that are closest to the bandgap. The optical transitions between VBM and CBM correspond to the basic absorption edges [82]. On the other hand, in ultraviolet, there is a sharp increase in absorption. In comparison, of both materials, the Ba_2AsNbO_6 has maximum absorption rather than the Ba_2AsTaO_6 compound. Understanding the refractive index n (ω) and extinction coefficient k(ω) of material aids in understanding its optoelectronic capabilities, which are vital for practical applications. Fig. 7 (c) shows the fluctuations of n (ω) versus photon energy (eV) for both examined Ba_2AsBO_6 (B═Nb, Ta) materials respectively. At 0 eV energy, the refractive index of Ba_2AsBO_6 (B═Nb, Ta) compounds is

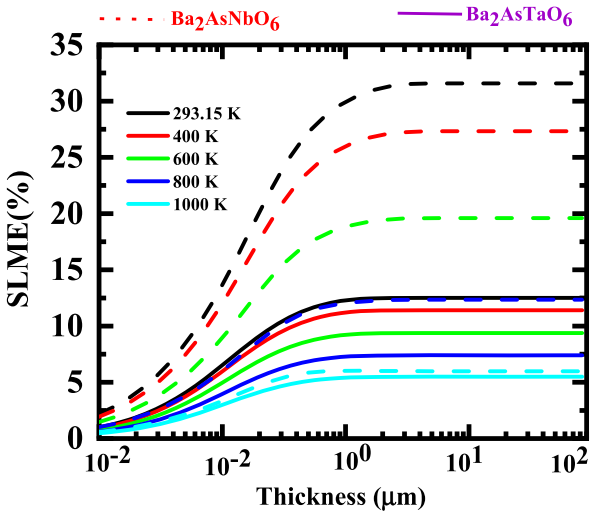

Fig. 9. Demonstrates the spectroscopic limited maximum efficiency against thickness with temperature variations for both Ba_2AsBO_6 (B═Nb, Ta) compounds correspondingly.

mentioned in Table 4 respectively, but the highest value of n (ω) for Ba_2AsBO_6 (B═Nb, Ta) are approximately 3 and 2.7 at 3.1 eV and 4.2 eV respectively. Lastly, we calculated the energy-related extinction coefficient, k(ω), which indicates the dampening of oscillation amplitude of the incoming electric field, is presented in Fig. 7 (d). At zero, there is no oscillation meanwhile by enhancing the energy (eV), the oscillations stated from the visible region as demonstrated in Fig. 7 (d). Fig. 8 (a) depicts the variance in optical conductivity for the materials examined against photon energy (eV) from 0 eV to 10 eV. For both compounds, the σ (ω) begins at around 1.8 eV and 2.3 eV and rises to 6000 $(cm)^{-1}$ and under 6000 $(cm)^{-1}$ at 5.5 eV and 6.3 eV, respectively. Our observation concluded that these materials can be employed in a variety of optoelectronic applications. The absorption coefficient α (ω) of the materials is another significant optical metric that shows how much light is absorbed by the material [83]. Fig. 8 (b) shows the energy-dependent absorption spectra of both Ba_2AsBO_6 (B═Nb, Ta) compounds against photon energy (eV). Absorption edges for Ba_2AsBO_6 (B═Nb, Ta) compounds can be seen at 1.5 eV and 2.5 eV respectively. For energy values larger than 3 eV, the substantial intensity of α (ω) is found, indicating that the examined materials could absorb visible and UV radiations. Well within energy spectrum of 0 eV–10 eV, the reflectivity R (ω) of the examined Ba_2AsBO_6 (B═Nb, Ta) materials have also been investigated and displayed in Fig. 8 (c). The reflectance of Ba_2AsBO_6 (B═Nb, Ta) at 0 eV energy is 0.131 and 0.15 correspondingly, indicating that the examined Ba_2AsBO_6 (B═Nb, Ta) materials are semiconducting. With raising photon energy, the reflectivity coefficient rises to a peak of 2 eV and 3.2 eV for Ba_2AsBO_6 (B═Nb, Ta), correspondingly. The function of electron energy Loss L (ω) is significant optical constant for determining the optical properties of substances. It provides data on the plasma frequency of the substances as well as the scattering of electrons traveling across them [82,84]. Fig. 8 (d) depicts the fluctuation of the loss of energy. The resonance situation is shown by the peaks in the graph of L (ω), which indicate the plasma frequency. Composites exhibit dielectric and semiconducting properties at energies above and below plasma frequency, correspondingly. Ba_2AsBO_6 (B═Nb, Ta) compounds have the greatest peaks about at 6.2 eV and 7.6 eV, correspondingly. The peaks in the electron energy loss coincide with the transition points of Ba_2AsBO_6 (B═Nb, Ta) from semiconducting to dielectric characteristics.

3.7. SLME analysis

The "spectroscopic limited maximum efficiency (SLME)" proposed by Liping Yu and Alex Zunger [88] may be used to evaluate the photovoltaic (PV) performance of a solid as an energetic absorber layer in a solo junction solar cell. SLME is a computational model that calculates the power conversion efficiency of a solar cell using the enhanced Shockley-Queisser model [89]. The ratio of the maximum output power density (P_{max}) to the total incoming solar energy density (P_{in}) is used to determine SLME. For SLME, the P_{max} may be computed using Eq. (11) [88,90,91], which gives the current-voltage (J-V) properties of the solar cell.

$$J_{SC} - J_0 \left(e^{\frac{eV}{K_B T}} - 1 \right) \tag{12}$$

Where J, J_{SC}, J_0, e, V, k, and T denote whole current density, short circuit current density, reverse saturation current density, elementary charge, potential over absorber layer, Boltzmann's constant, as well as gadget temperature, correspondingly. The absorptivity of the substance may be used to compute the J_{SC} and J_0 [90]. The key input parameters for analyzing the SLME are DFT computed absorption spectra, global solar spectra (AM1.5G), important (E_g), and direct allowable (E_{gda}) band gaps of the PV solid. $E_g = E_{gda}$ was used. The computed SLME (percent) for Ba_2AsBO_6 (B═Nb, Ta) materials at various temperatures and thickness values are shown in Fig. 9. We can observe that the material temperature, bandgap, and thickness of the PV absorber material have the most

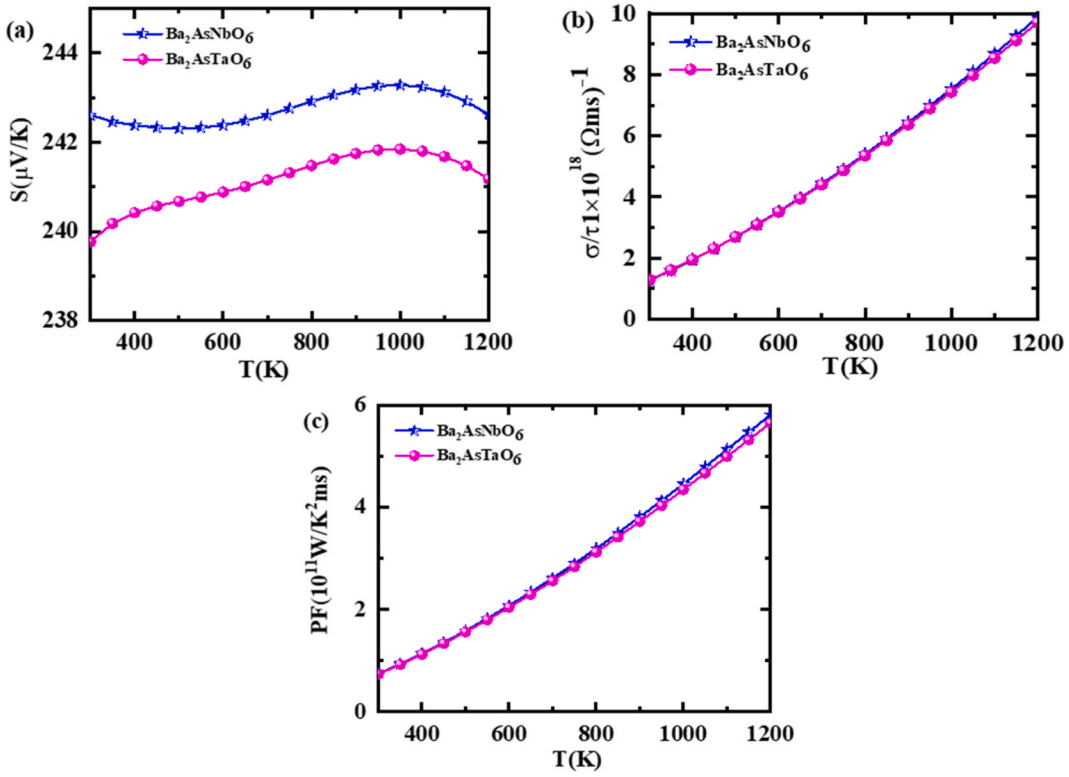

Fig. 10. Shows the (a) Seebeck coefficient (b) electrical conductivity (c) Power factor (PF) against temperature for both Ba_2AsBO_6 (B═Nb, Ta) compounds correspondingly.

impact on the SLME. When the device temperature is increased from 293.15K to 1000K, the SLME drops from 32 % (12.5 %) to 6 % (0.32 %) for Ba_2AsBO_6 (B═Nb, Ta) materials. Whereas it progressively surges with the thickness of the composite and remains constant after 1 m Ba_2AsTaO_6 has a lower SLME than Ba_2AsNaO_6 due to its higher band gap (2.49 eV) compared to Ba_2AsNbO_6 (1.49 eV). The Ba_2AsBO_6 (B═Nb, Ta) with a 32 % power conversion efficiency (PCE) screens and 12.5 % at 293.15 K, that is the real work temperature for a solar cell, as shown in Fig. 9. Ba_2AsNbO_6 has a PEC of 26.8 %, which is close to that of state-of-the-art inorganic PV cells (29.1 %) and the Shockley-Queisser (S-Q) efficiency limit of 33 % [92] assembly it a promising contender for single-junction solar cells.

3.8. Thermoelectric properties

The figure of merit (zT) is an imperative characteristic for determining the transport behavior of every object, evaluated using the electrical conductivity (ρ/τ), Seebeck coefficient (S), and thermal conductivity (κ/τ). We computed all these characteristics of the double perovskites Ba_2AsBO_2 (B═Nb, Ta) compounds against temperature chemical potential ($\boldsymbol{\mu}$–$\boldsymbol{\mu}_F$) eV over the effects of a diverse temperature, such as 300–1200 K and versus carrier's concentrations. Fig. 10(a–d) transport properties against the temperature for both studied double perovskites Ba_2AsBO_2 (B═Nb, Ta) compounds The S components are used to describe the types of dominant carriers in system. The S versus temperature examined with two temperatures for Ba_2AsBO_6 (B═Nb, Ta) compounds are round about 242.5 V/K, 239.3 V/K at 300 Kand at 1200 K 242.2 V/K and 241V/K correspondingly, as shown in Fig. 10 (a). At 300K, and 1200K temperatures, the measured values for the Seebeck coefficient for Nb is greater than Ta element due to its lower bandgap. The Seebeck coefficient must be high to have the highest thermoelectric performance. S is positive for p-type materials, but it is negative for n-type materials. Fig. 10 (a) depicts the fluctuation of S with temperature, indicating p-type nature with a positive S. Using perturbation theory [93], the computed effective masses (m*) (holes and electrons) for Ba_2AsBO_6 We assumed that the band structure remnants are identical to doping as well as the ($\boldsymbol{\mu}$–$\boldsymbol{\mu F}$) changes. Additionally, the relaxation duration energy independent Ba_2AsBO_6 (B═Nb, Ta) are (0.26) m^*_h, (1.68) m^*_e and (1.96) m^*_h (2.18) m^*_e, correspondingly. The larger Seebeck coefficient for electrons can also be attributed to $m^*e > m^*h$. The BoltzTrap algorithm was utilized to calculate transport characteristics in this study. Fig. 10 (b) demonstrates the (σ/τ) Ba_2AsBO_6 (B═Nb, Ta) versus temperature (K) correspondingly. At 300 K temperature, greatest value of σ/τ is 1.1×10^{18} $(\Omega ms)^{-1}$ for both compounds. By enhancing the T, the (σ/τ) linearly increased till 12000 K. the examined values of (σ/τ) for Ba_2AsBO_6 (B═Nb, Ta) compounds are 10×10^{18} $(\Omega ms)^{-1}$ respectively. Further, the computed PF for Ba_2AsBO_6 (B═Nb, Ta) compounds are shown in Fig. 10 (c). For both compounds, there is no variation at 300 K and similarly, at 1200 K. The computed values of the PF at 300 K and 1200 K are 0.89×10^{11} W/K^2ms and 5.9×10^{11} W/K^2ms respectively. The S against chemical potential over different

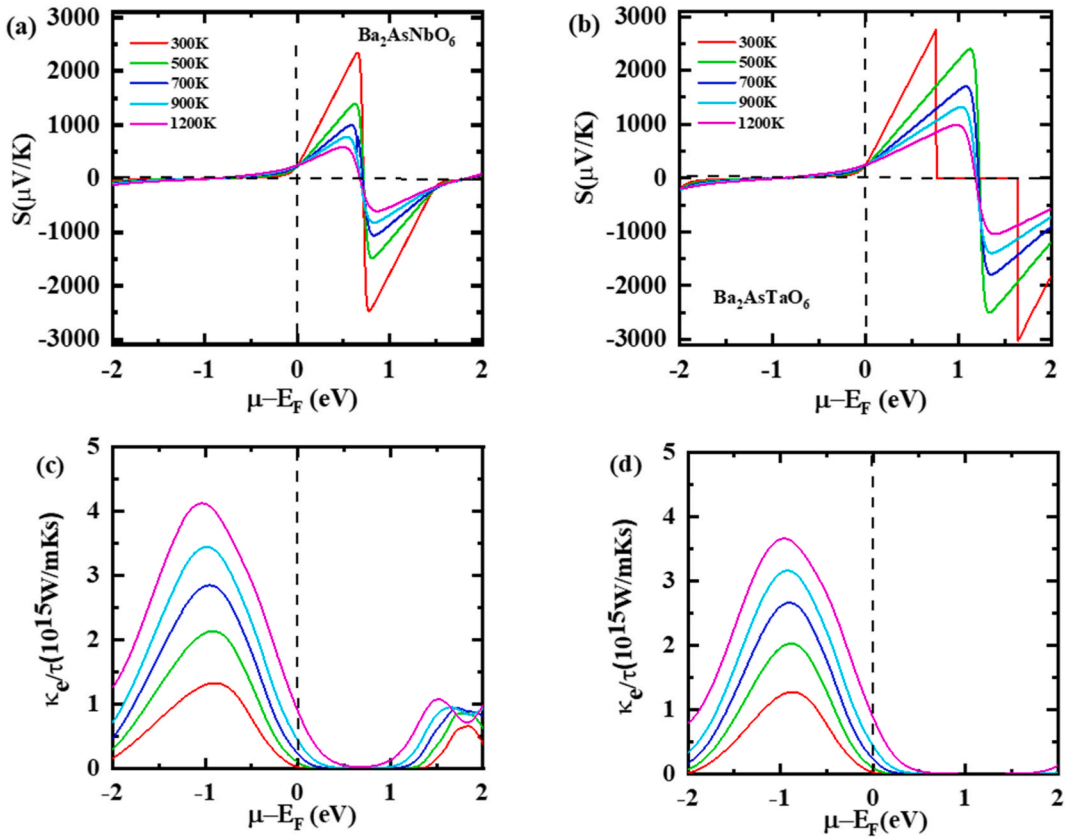

Fig. 11. Shows the (a, b) Seebeck coefficient (c, d) thermal conductivity against temperature for both Ba_2AsBO_6 (B═Nb, Ta) compounds correspondingly.

temperatures sure computed for two double perovskites for Ba_2AsBO_2 (B═Nb, Ta). The positive side indicated the n-type charge carriers and vice versa. We observed the maximum variations on the positive side but on the negative side, there are no variations as demonstrated in Fig. 11 (a, b). At 300 K there is a maximum magnitude of induced voltages as compared to 1200K. We analyzed by increasing the temperature-induced voltage is decreasing and for Ba_2AsBO_6 has greater voltages than Ba_2AsBO_6 compound. Highest values of σ/τ for holes than for electrons are shown in the behavior of the effective mass ($m^*e > m^*h$) since $\sigma/\tau = 1/m_{eff}$. The σ/τ decreased by increasing temperature. This suggests that intrinsic phonon scattering process dominates at higher temperatures. All parameters' values of double perovskites Ba_2AsBO_6 (B═Nb, Ta) at 300 are in Table 4. The electronic (κ/τ) is also considered against ($\mu-\mu F$) eV at different temperatures. We considered 300 K and 1200 K, there are larger variations in the side of the hole rather than the side of the electron. Thermal conductivity in Ba_2AsBO_6 compounds is greater than in Ba_2AsBO_6 compounds as demonstrated in Fig. 11 (c, d), which decreases as the temperature rises. This is due to the Wiedemann-Franz law, which describes link among electrical as well as electronic thermal conductivity (k_e/τ) as proportional to temperature.

Fig. 12(a–d) illustrates the electrical conductivity as well as power factor versus ($\mu-\mu F$) for Ba_2AsBO_6 (B═Nb, Ta), respectively. There is no difference in the σ/τ in the side of holes but we observed the maximum 17.5×10^{19} $(\Omega ms)^{-1}$ at 300 K and 1200 K. On the side of the electron, from 0 eV to 1.43 eV electrical conductivity remains zero which is associated to band-gap. Similarly, for Ba_2AsBO_6 there are also electronic band values that are related to the electronics band. At 300 K, there is 0.5×10^{11} W/K^2ms PF as compared to the 1200 K which is 7.8×10^{11} W/K^2ms in the Ba_2AsNbO_2 compound at −0.5 eV as shown in Fig. 12 (a). For the Ba_2AsTaO_2 compound at −0.5 eV with 300 K Fig. 12 (b). There is PF 0.65×10^{11} W/K^2ms and with 1200 K 7.35×10^{11} W/K^2ms respectively as illustrated in Fig. 12 (c, d). Fig. 13 (a, b) demonstrates the ZT versus ($\mu-\mu F$) eV for both materials of double perovskites and the ZT formula can be written as. $ZT = \sigma TS^2K$. ZT values advocate materials performance in thermal devices. We observed the ZT values are approximately 0.99 at 300 K and 0.83 at 1200 K for Ba_2AsBO_6. Similarly, for Ba_2AsBO_6 compound considered roundabout 0.97 at 300 K and 0.93 with 1200 K.

Morover, we have the transport properties versus N (e/uc) Ba_2AsBO_6 (B═Nb, Ta) compounds as shown in Figs. 14–16. To analyze the materials nature by n-type or p-type doping, we computed the S, σ/τ, κ/τ, PF, and ZT against carrier's concentrations N (e/uc) respectively. Here, positive presenting the holes doping and negative demonstrating the electrons doping in the materials. First, we considered the S versus N (e/uc) by electrons or holes there no dominated variations in the magnitude of induced voltages but when compered both the materials then could recognized the variation in Ba_2AsBO_6 for as compared to the Ba_2AsBO_6 compound from 0 N (e/uc) to −0.6 N (e/uc) as illustrated in Fig. 14 (a, b). Fig. 14(c and d) presents the κ/τ, at 300 K there is maximum value achieved in

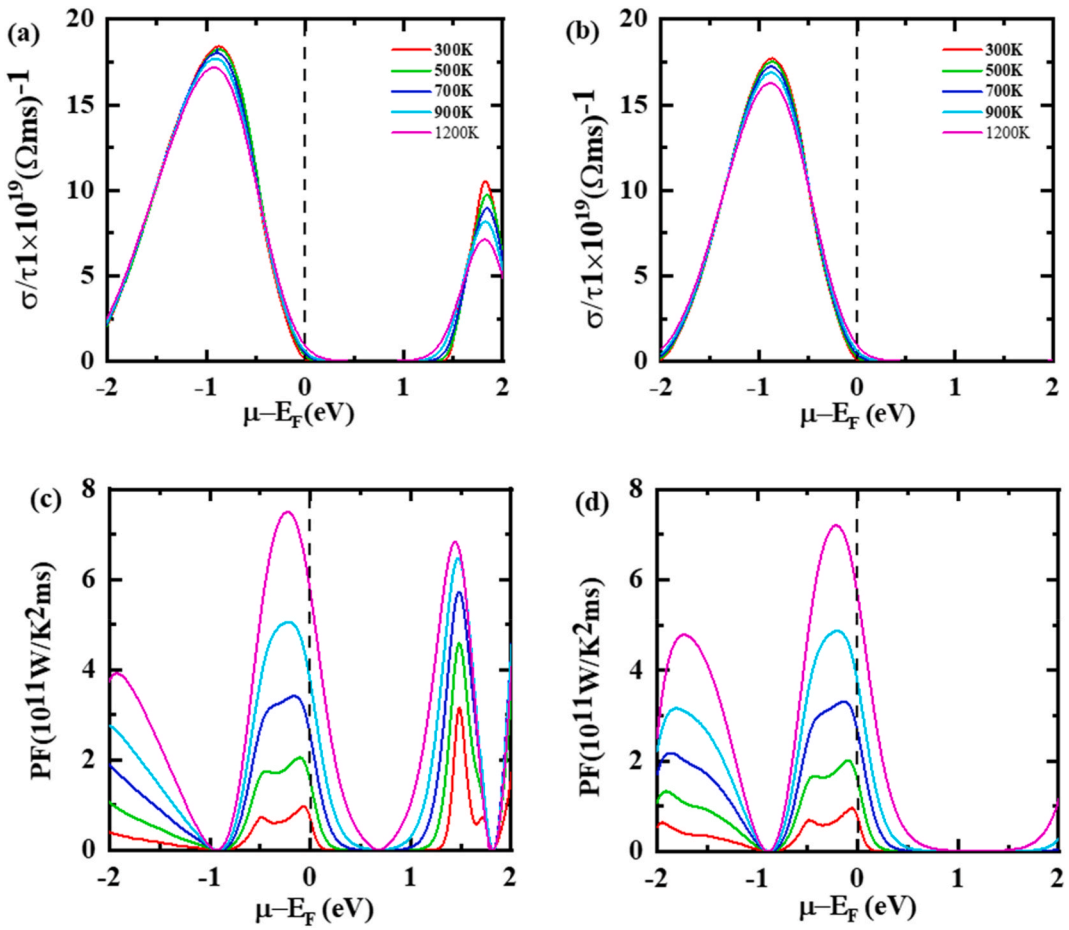

Fig. 12. Exhibits the (a, b) electrical conductivity (c, d) power factor against temperature (K) for both Ba_2AsBO_6 (B═Nb, Ta) compounds correspondingly.

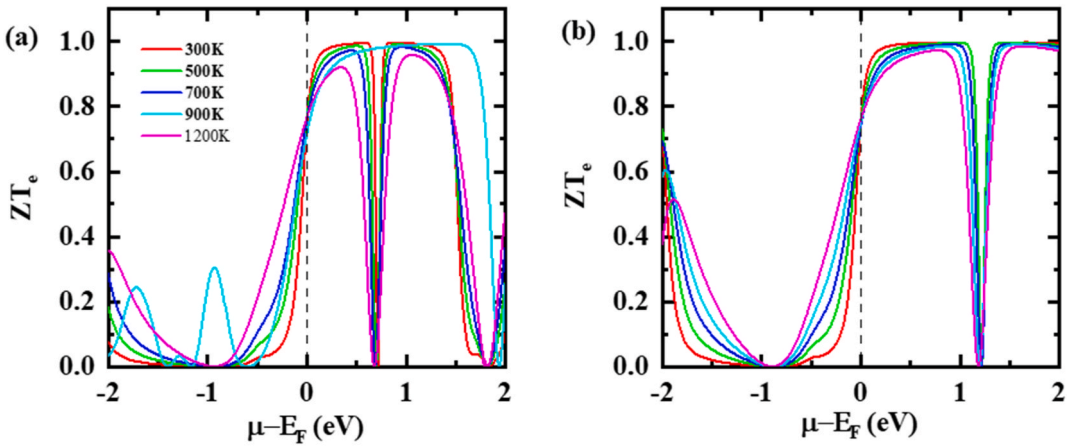

Fig. 13. Demonstrates the (a, b) figure of merits against temperature for both Ba_2AsBO_6 (B═Nb, Ta) compounds correspondingly.

positive side at 1 N (e/uc) about 1.2×10^{15} W/mK and further increasing the temperature thermal conductivity increased at 1.2 N (e/uc) with up to 4.1×10^{15} W/mK 3. 8×10^{15} W/mK, and 1.1×10^{15} W/mK values observed at 1200 K and 300 K for Ba_2AsBO_6 compound. In contrast to both compounds Ba_2AsTaO_6 compound has less thermal conductivity as compared to the Ba_2AsNbO_6 compound. Fig. 15(a–d) demonstrated the electrical conductivity and PF for double perovskites and examined the maximum values of

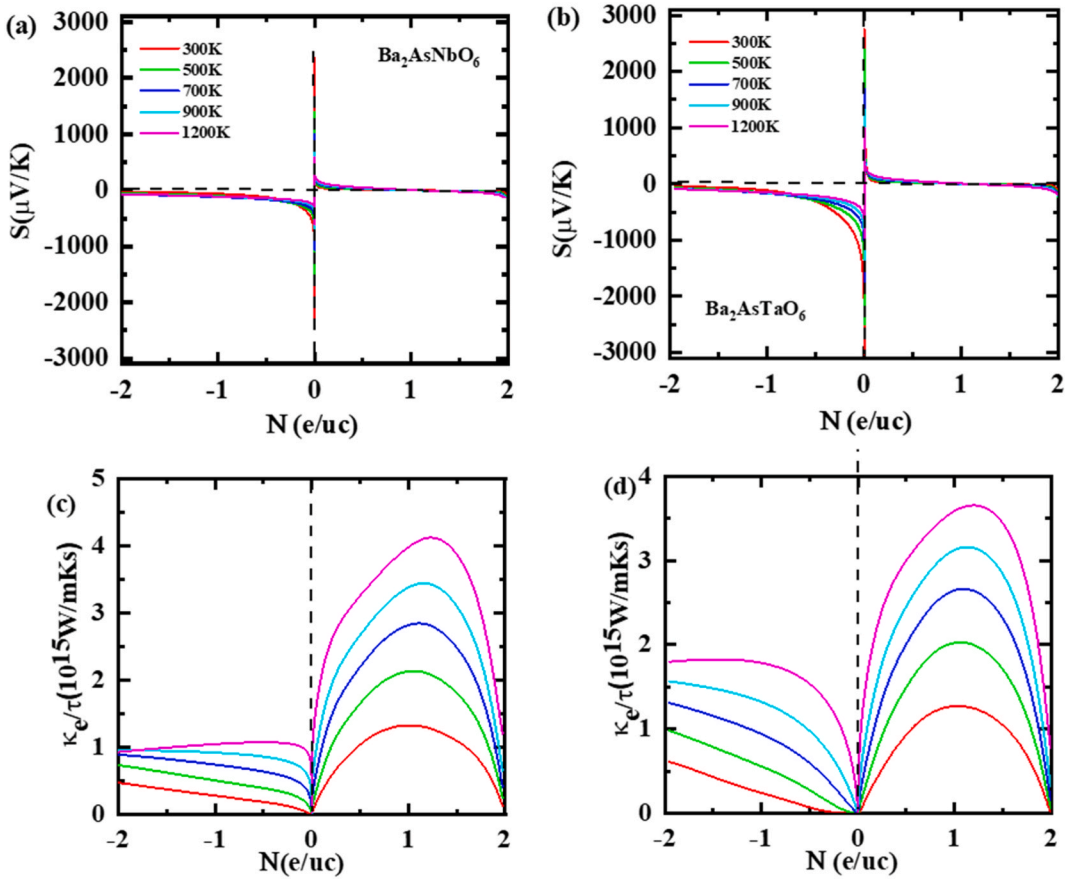

Fig. 14. Shows the (a, b) Seebeck coefficient (c, d) thermal conductivity against chemical potential for both Ba_2AsBO_6 (B═Nb, Ta) compounds correspondingly.

σ/τ are 18.5 × 10^{16} $(\Omega ms)^{-1}$ and 15.5 × 10^{16} $(\Omega ms)^{-1}$ at 1 N (e/uc) with 300 K and 1200K for Ba_2AsNbO_6 compound respectively. Moreover, for Ba_2AsTaO_6 compound the σ/τ values are observed up to 17.5 × 10^{16} $(\Omega ms)^{-1}$ and 16.2 × 10^{16} $(\Omega ms)^{-1}$ at 1 N (e/uc) with 300 K and 1200 K correspondingly. Fig. 15(c and d) presents the PF of double perovskites materials, examined the maximum PF with 1200 K at 0.25 N (e/uc) is 7.6 × 10^{11} W/K^2ms for Ba_2AsNbO_6 but with 300K the PF was lesson. On the other, for Ba_2AsTaO_6 material the maximum PF occurred in negative phase at 0.68 N (e/uc) with 1200 K. Overall, we can suggest by increasing temperature in doped materials the PF can increase in double perovskites materials. At 1 N (e/uc) in both Ba_2AsBO_6 (B═Nb, Ta) compounds, there is zero PF as shown in Fig. 14 (c, d). Fig. 16 (a, b) illustrates the ZT versus N (e/uc), we examined the maximum ZT for both compounds are 1 in pristine form. By p-type doping the ZT values suddenly decreased as compared to the n-type materials.

Thermal conductivity (*K*) is combination of *Kl* and *Ke*. Basically lattice thermal conductivity is phonon common excitation/vibrational/scattering in the material. It's excitation depending on the atomic structure of that specific atom as well as its bonds to other atoms in a solid. To determined the vibrational excitation, we calculated the Phonon vibration relied on the Boltzmann Transport Equation (BTE) joined to Relaxation Time Approximation (RTA). Fig. 17(a and b) demonstated the thermal conductivity by Slack eqaution for Ba_2AsBO_6 (B═Nb, Ta) compounds. we added this parameter (lattice thermal conductivity) in Fig. 17 (c), and then again calculate the figure of merits (ZT), from updated zT values, we analyzed the figure of merits (zT) decreased as compared to the perivious zT_e. However, "We analyzed that by increaseing the temperature the ZT values for both compounds increasing. At 1200 K, we examined the up to the 0.56 for both the compounds and also observed the same behavior. In future, experimetalist can synthesis these materials for optoelectronic and thermal devices.

4. Conclusion

We used DFT to consider the structural, mechanical, ELF electronics, optical, SLME, as well as transport properties of oxygen-based double perovskite Ba_2AsBO_6 (B═Nb, Ta) materials. The optimization, formation, cohesive energy, and phonon dispersion revealed the stability of Ba_2AsBO_6 (B═Nb, Ta) systems. To highlight the compounds' stability, ductility, and anisotropy, the studied mechanical characteristics indicates its applicability for device manufacturing. ELF elaborated the electrons movement from one state to and number of charge carriers. The electronic band structure calculation of Ba_2AsBO_6 (B═Nb, Ta) materials reveal that both are bandgap

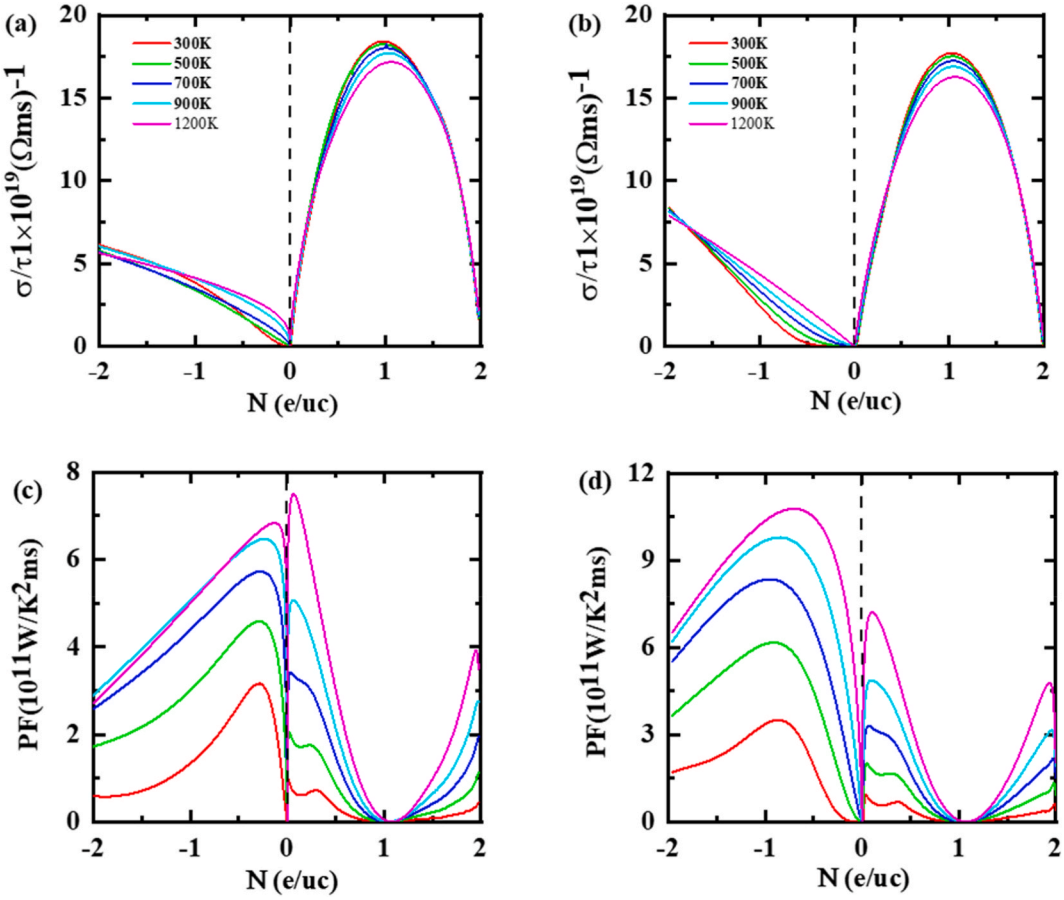

Fig. 15. Exhibits the (a, b) electrical conductivity (c, d) power factor against chemical potential for both Ba_2AsBO_6 (B═Nb, Ta) compounds correspondingly.

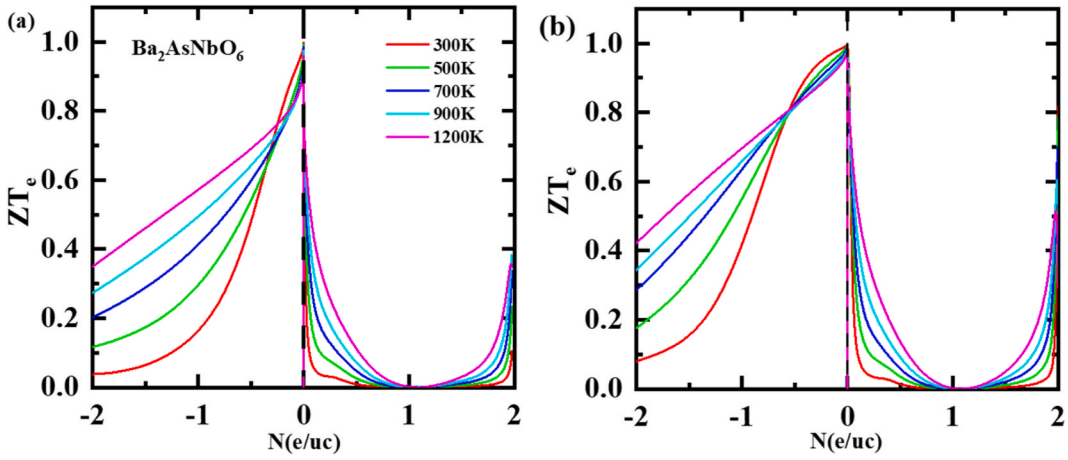

Fig. 16. Demonstrates the (a, b) figure of merits against temperature for Ba_2AsBO_6 (B═Nb, Ta) compounds correspondingly.

values 1.972 eV as well as 1.491 eV for Ba_2AsBO_6 (B═Nb, Ta) materials, respectively. In the optical properties, we examined that both compounds show excellent absorbing as well as minimum reflections in visible spectrum. SLME disclosed the highest absorptions for systems and Ba_2AsBO_6 (B═Nb, Ta) have a PEC of 26.8 %, revealing its fittingness for solar applications. In the transport properties, we estimated the PF and (zT) by employing BoltzTrap software. Calculated the zT values at 1200 K are 0.76 for both compounds and effective of electrons was greater than holes. The potential application of Ba_2AsBO_6 (B═Nb, Ta) compounds in optoelectronic as well

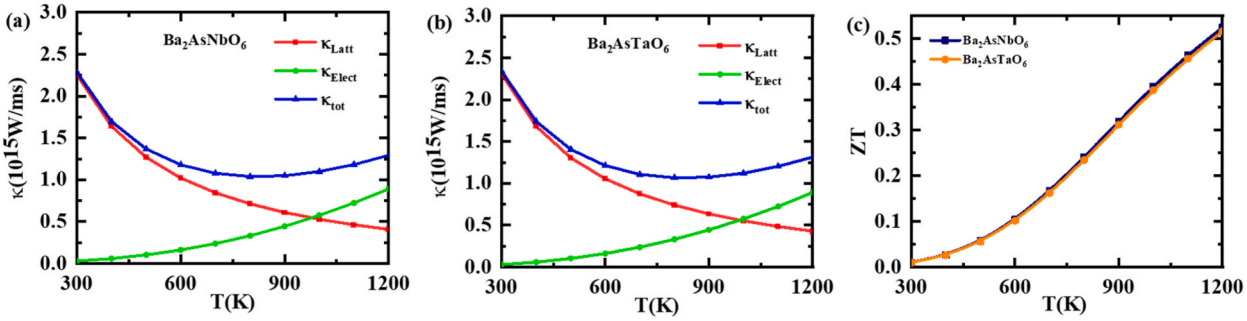

Fig. 17. Shows the (a) *Kl* and *Ke* of Ba_2AsNaO_6 (b) *Kl* and *Ke* of Ba_2AsNaO_6 (c) ZT against temperature compounds correspondingly.

as thermoelectric applications are confirmed by the fitting values of computed parameters such as band gap, absorption spectra, PF, as well as zT.

Data availability statement

Data will be available on request to corresponding author.

CRediT authorship contribution statement

Mumtaz Manzoor: Writing – original draft. **Debidatta Behera:** Writing – original draft. **Ramesh Sharma:** Writing – review & editing. **A.J.A. Moayad:** Investigation. **Abdullah A. Al-Kahtani:** Writing – review & editing. **Yedluri Anil Kumar:** Writing – review & editing.

Declaration of competing interest

The authors declare that they have no known competing financial interests or personal relationships that could have appeared to influence the work reported in this paper.

Acknowledgment

The authors are grateful to the Researchers Supporting Project number (RSP2024R266), King Saud University, Riyadh, Saudi Arabia for the financial support. M. M is supported by APVV-21-0272, VEGA-2/0070/21 Project, Slovakia.

References

[1] J. Suntivich, H.A. Gasteiger, N. Yabuuchi, H. Nakanishi, J.B. Goodenough, Y. Shao-Horn, Design principles for oxygen-reduction activity on perovskite oxide catalysts for fuel cells and metal–air batteries, Nat. Chem. 3 (2011) 546–550.
[2] S.D. Stranks, H.J. Snaith, Metal-halide perovskites for photovoltaic and light-emitting devices, Nat. Nanotechnol. 10 (2015) 391–402.
[3] M. Grätzel, The light and shade of perovskite solar cells, Nat. Mater. 13 (2014) 838–842.
[4] S. Vasala, M. Karppinen, A2B′ B ″O6 perovskites: a review, Prog. Solid State Chem. 43 (2015) 1–36.
[5] I. Grinberg, D.V. West, M. Torres, G. Gou, D.M. Stein, L. Wu, G. Chen, E.M. Gallo, A.R. Akbashev, P.K. Davies, Perovskite oxides for visible-light-absorbing ferroelectric and photovoltaic materials, Nature 503 (2013) 509–512.
[6] R. Ramesh, N.A. Spaldin, Multiferroics: progress and prospects in thin films, Nat. Mater. 6 (2007) 21–29.
[7] G. Rijnders, D.H. Blank, Build your own superlattice, Nature 433 (2005) 369–370.
[8] C. Ahn, K. Rabe, J.-M. Triscone, Ferroelectricity at the nanoscale: local polarization in oxide thin films and heterostructures, Science 303 (2004) 488–491.
[9] M.I. Hussain, R.A. Khalil, F. Hussain, Computational exploration of structural, electronic, and optical properties of novel combinations of inorganic ruddlesden–popper layered perovskites Bi2XO4 (X= Be, Mg) using tran and blaha-modified becke–johnson approach for optoelectronic applications, Energy Technol. 9 (2021) 2001026.
[10] M.I. Hussain, R.A. Khalil, F. Hussain, A.M. Rana, DFT-based insight into the magnetic and thermoelectric characteristics of XTaO3 (X= Rb, Fr) ternary perovskite oxides for optoelectronic applications, Int. J. Energy Res. 45 (2021) 2753–2765.
[11] Haq A. Ul, T.S. Ahmad, A. Ahmad, B.S. Almutairi, M. Amin, M. Khan, N. Ehsan, R. Sharma, A2LiGaI6 (A= Cs, Rb): new lead-free and direct bandgap halide double perovskites for IR application, Heliyon 9 (2023) e21702.
[12] M.A. Green, A. Ho-Baillie, H.J. Snaith, The emergence of perovskite solar cells, Nat. Photonics 8 (2014) 506–514.
[13] M.M. Lee, J. Teuscher, T. Miyasaka, T.N. Murakami, H.J. Snaith, Efficient hybrid solar cells based on meso-superstructured organometal halide perovskites, Science 338 (2012) 643–647.
[14] H.-S. Kim, C.-R. Lee, J.-H. Im, K.-B. Lee, T. Moehl, A. Marchioro, S.-J. Moon, R. Humphry-Baker, J.-H. Yum, J.E. Moser, Lead iodide perovskite sensitized all-solid-state submicron thin film mesoscopic solar cell with efficiency exceeding 9, Sci. Rep. 2 (2012) 591.
[15] M.N. Islam, J. Podder, Semiconductor to metallic transition in double halide perovskites Cs2AgBiCl6 through induced pressure: a DFT simulation for optoelectronic and photovoltaic applications, Heliyon 8 (2022) e10032.
[16] J.S. Manser, M.I. Saidaminov, J.A. Christians, O.M. Bakr, P.V. Kamat, Making and breaking of lead halide perovskites, Accounts Chem. Res. 49 (2016) 330–338.
[17] N. Espinosa, L. Serrano-Luján, A. Urbina, F.C. Krebs, Solution and vapour deposited lead perovskite solar cells: Ecotoxicity from a life cycle assessment perspective, Sol. Energy Mater. Sol. Cell. 137 (2015) 303–310.

[18] E.T. Hoke, D.J. Slotcavage, E.R. Dohner, A.R. Bowring, H.I. Karunadasa, M.D. Mcgehee, Reversible photo-induced trap formation in mixed-halide hybrid perovskites for photovoltaics, Chem. Sci. 6 (2015) 613–617.
[19] A. Babayigit, D. Duy Thanh, A. Ethirajan, J. Manca, M. Muller, H.-G. Boyen, B. Conings, Assessing the toxicity of Pb-and Sn-based perovskite solar cells in model organism Danio rerio, Sci. Rep. 6 (2016) 18721.
[20] Rasheed U., Imran M., Khalil R., Ashiq M. N., Mahata C., Hussain F., Theoretical exploration of site selective perovskites for the application of flexible optoresponsive memory devices, Theoretical Exploration of Site Selective Perovskites for the Application of Flexible Optoresponsive Memory Devices.
[21] E.A. Khera, C. Mahata, M. Imran, N.A. Niaz, F. Hussain, R.A. Khalil, U. Rasheed, Improved resistive switching characteristics of a multi-stacked HfO 2/Al 2 O 3/HfO 2 RRAM structure for neuromorphic and synaptic applications: experimental and computational study, RSC Adv. 12 (2022) 11649–11656.
[22] M.H. Ali, M.J. Islam, A. Kumer, M.S. Hossain, U. Chakma, D. Howlader, M.T. Islam, T. Hossain, Investigation of structural, electronic and optical properties of na 2 inagcl 6, k 2 inagcl 6, and rb 2 inagcl 6 lead-free halide double perovskites regarding with cs 2 inagcl 6 perovskites cell and a comparative study by dft functionals, Mater. Res. 24 (2021) e20210086.
[23] C. Eames, J.M. Frost, P.R. Barnes, B.C. O'regan, A. Walsh, M.S. Islam, Ionic transport in hybrid lead iodide perovskite solar cells, Nat. Commun. 6 (2015) 7497.
[24] S. Meloni, T. Moehl, W. Tress, M. Franckevičius, M. Saliba, Y.H. Lee, P. Gao, M.K. Nazeeruddin, S.M. Zakeeruddin, U. Rothlisberger, Ionic polarization-induced current–voltage hysteresis in CH3NH3PbX3 perovskite solar cells, Nat. Commun. 7 (2016) 10334.
[25] C.C. Stoumpos, C.D. Malliakas, M.G. Kanatzidis, Semiconducting tin and lead iodide perovskites with organic cations: phase transitions, high mobilities, and near-infrared photoluminescent properties, Inorg. Chem. 52 (2013) 9019–9038.
[26] T. Baikie, Y. Fang, J.M. Kadro, M. Schreyer, F. Wei, S.G. Mhaisalkar, M. Graetzel, T.J. White, Synthesis and crystal chemistry of the hybrid perovskite (CH 3 NH 3) PbI 3 for solid-state sensitised solar cell applications, J. Mater. Chem. A 1 (2013) 5628–5641.
[27] S. Nazir, N. Noor, M. Manzoor, A. Dahshan, Ab-initio simulations of Li-based double perovksites A2LiInBr6 (A= Rb, Cs) for solar cell applications, Chem. Phys. Lett. 798 (2022) 139612.
[28] M.W. Iqbal, M. Manzoor, N. Noor, I. Rehman, N. Mushahid, S. Aftab, Y.M. Alanazi, H. Ullah, A.M. Afzal, Tuning of the electronic bandgap of lead-free double perovskites K2AgBiX6 (X= Cl, Br) for solar cells applications and their thermoelectric characteristics, Sol. Energy 239 (2022) 234–241.
[29] S. Maqsood, A.U. Rahman, M. Nawaz, M.A. Ahmad, M. Manzoor, N. Noor, S.A. Abdelmohsen, Ab-initio method to investigate organic halide based double perovskites (CH3NH3) 2AgMBr6 (M= Sb, Bi) for opto-electronic applications, J. Mater. Res. Technol. 17 (2022) 649–657.
[30] R. Nechache, C. Harnagea, S. Li, L. Cardenas, W. Huang, J. Chakrabartty, F. Rosei, Bandgap tuning of multiferroic oxide solar cells, Nat. Photonics 9 (2015) 61–67.
[31] R.F. Berger, J.B. Neaton, Computational design of low-band-gap double perovskites, Phys. Rev. B 86 (2012) 165211.
[32] Q. Sun, J. Wang, W.J. Yin, Y. Yan, Bandgap engineering of stable lead-free oxide double perovskites for photovoltaics, Adv. Mater. 30 (2018) 1705901.
[33] W.-J. Yin, B. Weng, J. Ge, Q. Sun, Z. Li, Y. Yan, Oxide perovskites, double perovskites and derivatives for electrocatalysis, photocatalysis, and photovoltaics, Energy Environ. Sci. 12 (2019) 442–462.
[34] E.T. Mcclure, M.R. Ball, W. Windl, P.M. Woodward, Cs2AgBiX6 (X= Br, Cl): new visible light absorbing, lead-free halide perovskite semiconductors, Chem. Mater. 28 (2016) 1348–1354.
[35] G. Volonakis, M.R. Filip, A.A. Haghighirad, N. Sakai, B. Wenger, H.J. Snaith, F. Giustino, Lead-free halide double perovskites via heterovalent substitution of noble metals, J. Phys. Chem. Lett. 7 (2016) 1254–1259.
[36] G. Volonakis, A.A. Haghighirad, R.L. Milot, W.H. Sio, M.R. Filip, B. Wenger, M.B. Johnston, L.M. Herz, H.J. Snaith, F. Giustino, Cs2InAgCl6: a new lead-free halide double perovskite with direct band gap, J. Phys. Chem. Lett. 8 (2017) 772–778.
[37] G. Volonakis, N. Sakai, H.J. Snaith, F. Giustino, Oxide analogs of halide perovskites and the new semiconductor Ba2AgIO6, J. Phys. Chem. Lett. 10 (2019) 1722–1728.
[38] A. Soni, K. Bhamu, J. Sahariya, Investigating effect of strain on electronic and optical properties of lead free double perovskite Cs2AgInCl6 solar cell compound: a first principle calculation, J. Alloys Compd. 817 (2020) 152758.
[39] S.M. Alay-E-Abbas, G. Abbas, W. Zulfiqar, M. Sajjad, N. Singh, J.A. Larsson, Structure inversion asymmetry enhanced electronic structure and electrical transport in 2D A3SnO (A= Ca, Sr, and Ba) anti-perovskite monolayers, Nano Res. 16 (2023) 1779–1791.
[40] A. Sharan, M. Sajjad, D.J. Singh, N. Singh, Two-dimensional ternary chalcogenides Fe X 2 Y 4 (X= Ga, In; Y= S, Se, Te): promising materials for sustainable energy, Phys. Rev. Mater. 6 (2022) 094005.
[41] M. Zanib, M.W. Iqbal, M. Manzoor, M. Asghar, R. Sharma, N.N. Ahmad, S.M. Wabaidur, M.A. Habila, S.A. Abdelmohsen, A.M. Abdelbacki, A DFT investigation of mechanical, optical and thermoelectric properties of double perovskites K2AgAsX6 (X= Cl, Br) halides, Mater. Sci. Eng. B 295 (2023) 116604.
[42] M.W. Iqbal, M. Manzoor, S. Gouadria, M. Asghar, M. Zainab, N.N. Ahamd, S. Aftab, R. Sharma, T. Zahid, DFT insights on the opto-electronic and thermoelectric properties of double perovskites K2AgSbX6 (X= Cl, Br) via halides substitutions for solar cell applications, Mater. Sci. Eng. B 290 (2023) 116338.
[43] D. Behera, M. Manzoor, R. Sharma, M.M. Salah, I. Stich, S.K. Mukherjee, A comprehensive first-principles investigation of SnTiO3 perovskite for optoelectronic and thermoelectric applications, Crystals 13 (2023) 408.
[44] M. Manzoor, D. Behera, R. Sharma, M.W. Iqbal, S.K. Mukherjee, R. Khenata, S.S. Alarfaji, H.A. Alzahrani, Investigation of the structural, mechanical, optoelectronic and, thermoelectric characteristics of cubic GeTiO3: an ab initio study, Mater. Today Commun. 34 (2023) 105053.
[45] M. Manzoor, M.W. Iqbal, N.A. Noor, H. Ullah, R. Sharma, S.S. Alarfaji, Exploring the structural, electronic, optical, and thermoelectric properties of potassium-based double perovskites K2AgXI6 (X= Sb, Bi) compounds: a DFT study, Mater. Sci. Eng., B 287 (2023) 116122.
[46] S. Tyagi, R. Chaurasiya, N. Singh, A. Dixit, Strain engineered thermodynamic stability, electronic and thermoelectric characteristics of TiB2 and ZrB2 monolayers, Phys. E Low-dimens. Syst. Nanostruct. 145 (2023) 115477.
[47] A. Yadav, J. Kangsabanik, N. Singh, A. Alam, Novel two-dimensional MA2N4 materials for photovoltaic and spintronic applications, J. Phys. Chem. Lett. 12 (2021) 10120–10127.
[48] M.I. Hussain, R.A. Khalil, S. Boota, F. Hussain, M. Imran, G. Murtaza, A.M. Rana, M. Sattar, The structural, electronic and dynamical investigations of NdMn2O5 and La2CoMnO6 for optoelectronic applications: a first principles study, Optik 204 (2020) 164165.
[49] R.A. Khalil, M.I. Hussain, A. Batool, F. Hussain, A.M. Rana, N. Luqman, Computational study of TbMn2O5 and Tb2MnCoO6 to probe the structural, vibrational and optoelectronic properties using PBE+ U functional, Optik 241 (2021) 166835.
[50] S.V. Trukhanov, I. Troyanchuk, M. Hervieu, H. Szymczak, K. Bärner, Magnetic and electrical properties of L BaMn 2 O 6− γ (L= Pr, Nd, Sm, Eu, Gd, Tb) manganites, Phys. Rev. B. 66 (2002) 184424.
[51] K. Momma, F. Izumi, VESTA 3 for three-dimensional visualization of crystal, volumetric and morphology data, J. Appl. Crystallogr. 44 (2011) 1272–1276.
[52] P. Blaha, K. Schwarz, G.K. Madsen, D. Kvasnicka, J. Luitz, wien2k, an Augmented Plane Wave+ Local Orbitals Program for Calculating Crystal Properties, vol. 60, 2001.
[53] J.P. Perdew, K. Burke, M. Ernzerhof, Generalized gradient approximation made simple, Phys. Rev. Lett. 77 (1996) 3865.
[54] M. Raïâ, R. Masrour, M. Hamedoun, J. Kharbach, A. Rezzouk, A. Hourmatallah, N. Benzakour, K. Bouslykhane, Half-metalicity, mechanical, optical, thermodynamic, and thermoelectric properties of full Heusler alloys Co2TiZ (Z= Si; Ge; Sn), Opt. Quant. Electron. 55 (2023) 512.
[55] A. Azouaoui, A. Harbi, M. Moutaabbid, M. Idiri, A. Eddiai, N. Benzakour, A. Hourmatallah, K. Bouslykhane, R. Masrour, A. Rezzouk, First-principle investigation of LiSrX (X= P and As) half-Heusler semiconductor compounds, Indian J. Phys. 97 (2023) 1727–1737.
[56] G.K. Madsen, D.J. Singh, BoltzTraP, A code for calculating band-structure dependent quantities, Comput. Phys. Commun. 175 (2006) 67–71.
[57] A. Azouaoui, A. Harbi, M. Moutaabbid, N. Benzakour, A. Hourmatallah, K. Bouslykhane, R. Masrour, A. Chahboun, Influence of pressure on structural stability and physical properties of NaCaZ (Z= N, P and As) half-Heusler semiconductor materials, Int. J. Mod. Phys. B 38 (2024) 2450122.
[58] A. Ali, M.S. Khan, M. Irfan, G. Khan, B. Gul, S. Azam, H. Haider, A. Ullah, M.R. Karim, I.A. Alnaser, First-principles study of electronic, optical, magnetic, and thermoelectric properties of novel Sr2UXO6 (X= Mn, Zn) double perovskites, Chem. Phys. Lett. 835 (2024) 141019.
[59] K. Bhamu, A. Soni, J. Sahariya, Revealing optoelectronic and transport properties of potential perovskites Cs2PdX6 (X= Cl, Br): a probe from density functional theory (DFT), Sol. Energy 162 (2018) 336–343.

[60] D. Rai, A. Shankar, M. Ghimire, R. Thapa, The electronic, magnetic and optical properties of double perovskite A2FeReO6 (A= Sr, Ba) from first principles approach, Comput. Mater. Sci. 101 (2015) 313–320.
[61] M. Raïâ, R. Masrour, M. Hamedoun, J. Kharbach, A. Rezzouk, A. Hourmatallah, N. Benzakour, K. Bouslykhane, Diluted effect on the structural, magnetic, electronic, thermodynamic, optical and thermoelectric properties of the Heusler alloys Co2Fe1− xTixGa: GGA and GGA+ U approaches, Opt. Quant. Electron. 55 (2023) 140.
[62] F. Mouhat, F.-X. Coudert, Necessary and sufficient elastic stability conditions in various crystal systems, Phys. Rev. B 90 (2014) 224104.
[63] M.E. Eberhart, T.E. Jones, Cauchy pressure and the generalized bonding model for nonmagnetic bcc transition metals, Phys. Rev. B 86 (2012) 134106.
[64] M. Raïâ, R. Masrour, M. Hamedoun, J. Kharbach, A. Rezzouk, A. Hourmatallah, N. Benzakour, K. Bouslykhane, Structural, electronic, magnetic, elastic, thermoelectric, and thermal properties of Co2FeGa1− xSix Heusler alloys: first-principles calculations, J. Supercond. Nov. Magnetism 36 (2023) 349–365.
[65] I.A. Masrour R. Elkoua, Structural, thermodynamics, optical, electronic, magnetic and thermoelectric properties of Heusler Ni2MnGa: an ab initio calculations, Opt. Quant. Electron. 54 (2022) 667.
[66] M. Born, K. Huang, Dynamical Theory of Crystal Lattices, Oxford university press, 1996.
[67] B. Holm, R. Ahuja, Ab initio calculation of elastic constants of SiO 2 stishovite and α-quartz, J. Chem. Phys. 111 (1999) 2071–2074.
[68] A. Reuß, Berechnung der fließgrenze von mischkristallen auf grund der plastizitätsbedingung für einkristalle, ZAMM-Journal of Applied Mathematics and Mechanics/Zeitschrift für Angewandte Mathematik und Mechanik 9 (1929) 49–58.
[69] E. Anastassakis, E. Liarokapis, Polycrystalline Si under strain: elastic and lattice-dynamical considerations, J. Appl. Phys. 62 (1987) 3346–3352.
[70] H. Karwasara, K. Bhamu, S.G. Kang, A. Kushwaha, D. Rai, S. Sappati, J. Sahariya, A. Soni, Ab-initio investigations for structural, mechanical, optoelectronic, and thermoelectric properties of Ba2SbXO6 (XNb, Ta) compounds, J. Alloys Compd. 893 (2022) 162332.
[71] K. Bhamu, S.G. Kang, A. Kushwaha, D. Rai, S. Sappati, J. Sahariya, A. Soni, Ab-initio investigations for structural. Mechanical, Optoelectronic, and Thermoelectric Properties of Ba2SbXO6 (X= Nb, Ta) Compounds, arXiv preprint arXiv:2105.10976, 2021.
[72] S. Pugh, XCII. Relations between the elastic moduli and the plastic properties of polycrystalline pure metals, London, Edinburgh Dublin Phil. Mag. J. Sci. 45 (1954) 823–843.
[73] K. Haddadi, A. Bouhemadou, L. Louail, Y. Medkour, Structural, elastic and electronic properties of XNCa3 (X= Ge, Sn and Pb) compounds, Solid State Commun. 149 (2009) 619–624.
[74] E. Schreiber, O.L. Anderson, N. Soga, J.F. Bell, Elastic Constants and Their Measurement, 1975.
[75] C. Kube, Elastic anisotropy of crystals, AIP Adv. 6 (2016) 095209.
[76] C. Zener, Elasticity and an Elasticity of Metals, University of Chicago Press, Chicago, 1948.
[77] M. Al-Hattab, K. Rahmani, Thermodynamic, optical, and morphological studies of the Cs2AgBiX6 double perovskites (X= Cl, Br, and I): insights from DFT study, J. Alloys Compd. 960 (2023) 170650.
[78] C. Ambrosch-Draxl, J.O. Sofo, Linear optical properties of solids within the full-potential linearized augmented planewave method, Comput. Phys. Commun. 175 (2006) 1–14.
[79] M.Y. Raïâ, R. Masrour, M. Hamedoun, J. Kharbach, A. Rezzouk, A. Hourmatallah, N. Benzakour, K. Bouslykhane, Stability, magnetic, electronic, elastic, thermodynamic, optical, and thermoelectric properties of Co2TiSn, Co2ZrSn and Co2HfSn Heusler alloys from calculations using generalized gradient approximation techniques, J. Mater. Sci. Mater. Electron. 33 (2022) 20229–20256.
[80] D.R. Penn, Wave-number-dependent dielectric function of semiconductors, Phys. Rev. 128 (1962) 2093.
[81] R. Abt, C. Ambrosch-Draxl, P. Knoll, Optical response of high temperature superconductors by full potential LAPW band structure calculations, Phys. B Condens. Matter 194 (1994) 1451–1452.
[82] M. Al-Hattab, L.H. Moudou, Y. Chrafih, K. Rahmani, M. Khenfouch, O. Bajjou, First-principles calculation of the structural, electronic and optical properties of GaSe_ (1-x) S_ (x)(x= 0, 0.25, 0.5 and 1) compounds, Advances in Materials and Processing Technologies 8 (2022) 2731–2743.
[83] D. Behera, M. Manzoor, M.W. Iqbal, S. Lakra, S. Mukherjee, Revealing excellent electronic, optical, and thermoelectric behavior of Eu based EuAg2Y2 (Y= S/Se): for solar cell applications, Computational Condensed Matter 32 (2022) e00723.
[84] D. Behera, M. Manzoor, M. Maharana, M.W. Iqbal, T. Zahid, S. Lakra, S. Mukherjee, S.S. Alarfaji, Structural, electronic, optical, and thermoelectric response of zintl phase AAg2S2 (A= Sr/Ba) compounds for renewable energy applications, Phys. B Condens. Matter 649 (2023) 414446.
[85] M.Z. Kazim, M. Yaseen, S.A. Aldaghfag, M. Ishfaq, M. Nazar, M. Zahid, R. Neffati, DFT study of optoelectronic and thermoelectric properties of cubic Ba2ZrMO6 (M= Ce, Ti) double perovskites, J. Solid State Chem. 315 (2022) 123419.
[86] M. Manzoor, M. Hussain, M. Aslam, B. Evgeny, R. Sharma, A.S. Alshomrany, N. Sfina, Tailoring the physical, optoelectronic and transport properties of novel lead-free Sodium perovskites Na2TeX6 (X= Cl, Br, I) using DFT computation for photovoltaic and thermal devices, Chin. J. Phys. (2024).
[87] M. Al-Hattab, Y. Chrafih, E. Oublal, M. Sahal, O. Bajjou, K. Rahmani, Ab initio investigation for solar technology on the optical and electronic properties of double perovskites Cs2AgBiX6 (X= Cl, Br, I), ECS Journal of Solid State Science and Technology. 12 (2023) 094004.
[88] L. Zunger A. Yu, Identification of potential photovoltaic absorbers based on first-principles spectroscopic screening of materials, Phys. Rev. Lett. 108 (2012) 068701.
[89] M. Al-Hattab, L.H. Moudou, M. Khenfouch, O. Bajjou, K. Rahmani, Structural, electronic, and elastic properties of different polytypes of GaSe lamellar materials under compressive stress: insights from a DFT study, J. Nanoparticle Res. 24 (2022) 219.
[90] M. Bercx, N. Sarmadian, R. Saniz, B. Partoens, D. Lamoen, First-principles analysis of the spectroscopic limited maximum efficiency of photovoltaic absorber layers for CuAu-like chalcogenides and silicon, Phys. Chem. Chem. Phys. 18 (2016) 20542–20549.
[91] H.-J. Feng, K. Wu, Z.-Y. Deng, Predicting inorganic photovoltaic materials with efficiencies> 26% via structure-relevant machine learning and density functional calculations, Cell Reports Physical Science 1 (2020).
[92] J. Wang, V. Zardetto, K. Datta, D. Zhang, M.M. Wienk, R.A. Janssen, 16.8% Monolithic all-perovskite triple-junction solar cells via a universal two-step solution process, Nat. Commun. 11 (2020) 5254.
[93] O. Rubel, F. Tran, X. Rocquefelte, P. Blaha, Perturbation approach to ab initio effective mass calculations, Comput. Phys. Commun. 261 (2021) 107648.